Large-Scale Cloud Properties and Radiative Fluxes over Darwin during Tropical Warm Pool – International Cloud Experiment

P. Minnis, L. Nguyen, and W.L. Smith, Jr.
National Aeronautics and Space Administration/Langley Research Center
Hampton, Virginia

R. Palikonka, J.K. Ayers, D.R. Doelling, M.L. Nordeen, D. Spangenberg, D.N. Phan, and M. Khaiyer
Analytical Services & Materials, Inc.
Hampton, Virginia

G.G. Mace
University of Utah
Salt Lake City, Utah

Introduction

The Atmospheric Radiation Measurement (ARM) Program-sponsored Tropical Warm Pool - International Cloud Experiment (TWP-ICE) was conducted from 23 January - 13 February 2006 in Darwin, Australia, to characterize the properties of tropical cirrus and the convection that leads to their formation. An important component of that characterization is wide-area coverage provided by satellites. This study provides preliminary analyses of radiative fluxes and cloud properties derived from imagers on two geostationary satellites (GEOsat), MTSAT-1R and FY-2C, and from the low earth-orbit Advanced Very High Resolution Radiometers (AVHRR) on National Oceanic and Atmospheric Administration (NOAA)-15, 16, 17, and 18, and the Moderate Resolution Imaging Spectroradiometer (MODIS) on Aqua and Terra.

Data and Methodology

Data from the imagers on the MTSAT-1R and FY-2C consist of 5- and 4-km visible (VIS) (0.7 μm), solar-infrared (3.8 μm), infrared (IR) (10.8 μm), and split-window (12.0 μm) bands, respectively. They are taken hourly and staggered at the half hour. Data from similar channels on the 1-km MODIS and 4-km AVHRR are taken from a given low earth-orbit satellite twice daily, 12 hours apart. The Darwin domain extends from 5°S to 17°S and from 125°E to 136°E. This domain is a subset of the MTSAT-1R

greater TWP domain, which covers the area between 10°N and 20°S and 120°E and 180°E. The 6-hourly NOAA Global Forecast Systems numerical weather analyses provide vertical profiles of temperature and humidity over the domain. These are interpolated in time and space to match the 0.5° satellite analysis resolution and the temporal sampling of the particular satellite. The profiles are used to convert the retrieved cloud temperature Tc to cloud height zc and correct radiances for atmospheric attenuation. Surface-type, clear-sky albedo, and surface emissivity maps are used to estimate the cloud-free radiances for a given scene as described by Minnis et al. (2002c, 2004) cloudy pixel.

The cloudy pixels are analyzed the Visible Infrared Solar-Infrared Split-window Technique (VISST) during the daytime and the Solar-Infrared Infrared Split-window Technique (SIST) during the night (Minnis et al. 1995, 1998). VISST derives cloud temperature, top and base heights, optical depth (OD), particle phase, effective ice particle diameter (De), ice water path, effective liquid drop radius, and liquid water path. The SIST retrieves similar parameters except that the particle sizes, optical depths, and water paths are limited to optically thin clouds. Default values are used in thick cloud cases.

Figure 1 shows examples of the imagery taken within a 1.5-hour period over the domain from four different satellites. The images are presented in pseudocolor with red, green, and blue intensities determined by the 10.8 μm (IR) brightness temperatures, differences between the IR and 3.8-μm brightness temperatures, and the visible reflectances, respectively. The *Aqua* MODIS image shows the most detail, followed by the AVHRR, MTSAT, and FY2C images. Errors in navigation as large as 6 pixels were found in the FY2C and MTSAT images. Empirical corrections were developed and applied to account for the offsets. Some residual errors are likely. Compared to their MTSAT counterparts, the FY2C pixels appear to be “smeared” over a larger area despite the greater nominal resolution. That smearing effect affects the quality of the retrievals.

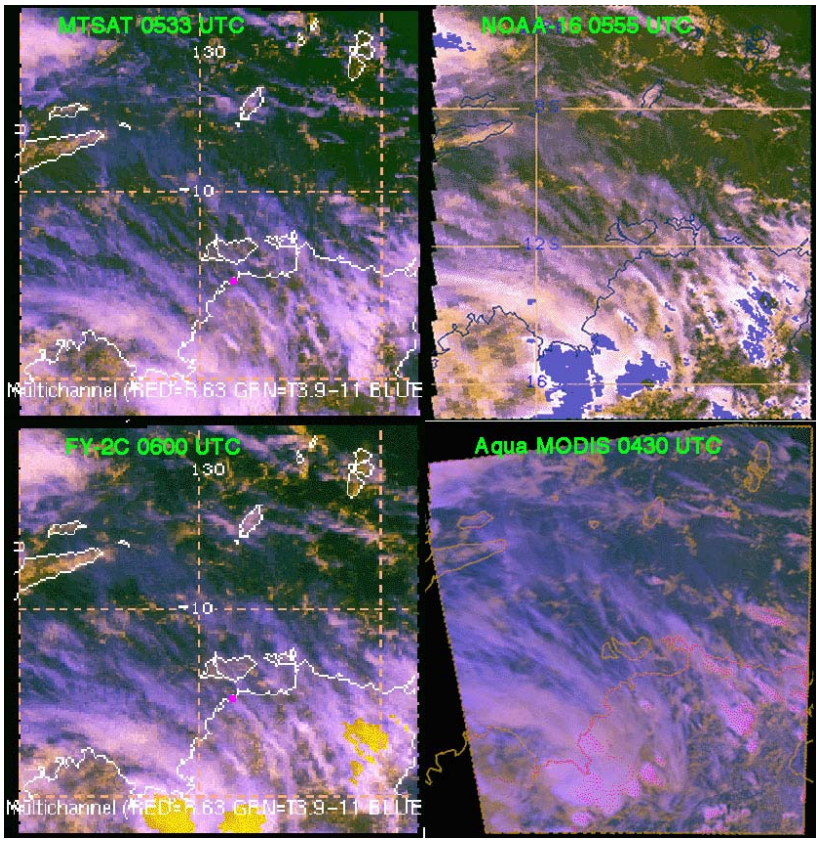

Figure 1. RGB images from flight day, 25 January 2006, for four satellites around 0515 Universal Time Coordinates (UTC). Each has a unique perspective.

Although the VIS channels on the two GEO satellites have a significantly greater central wavelength (0.72 μm compared to 0.64 μm) than the MODIS, they are treated as if they are equivalent to the MODIS VIS channel. The actual spectral filter functions and, therefore, the central wavelengths for the FY2C are not available and are assumed here to be the same as those for the corresponding MTSAT channels. To minimize additional effects of the spectral differences, all of the GEOsat channels were intercalibrated over ocean to their *Aqua* MODIS counterparts following the approach of Minnis et al. (2002a, b). Figure 2 shows the correlations and a variety of linear fits between the MTSAT and FY2C VIS channels and the *Aqua* MODIS VIS channel during the TWP-ICE period. The MODIS radiance L_M, ($Wm^{-2}sr^{-1}\mu m^{-1}$) is plotted as a function of the GEOsat squared 8-bit count, D^2. Using simple linear regression for MTSAT and FY2C,

$$L_M = 0.01143(D^2 + 1440) \quad (1)$$

and

$$L_M = 0.01008(D^2 + 1016), \quad (2)$$

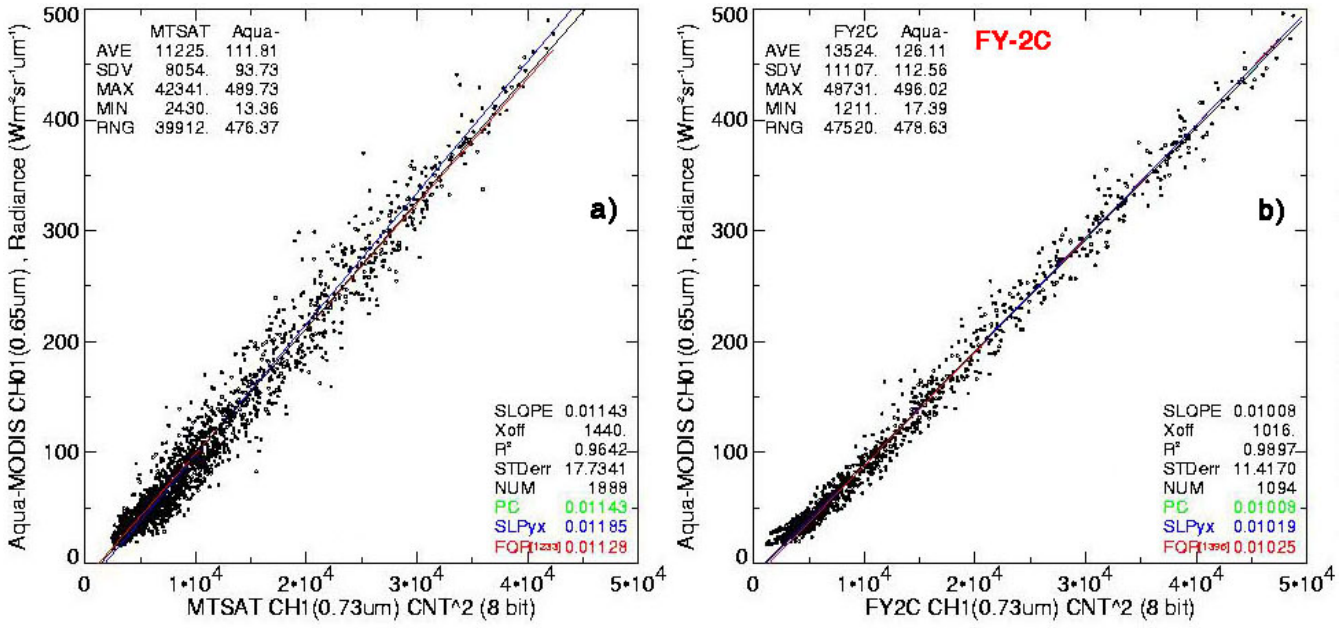

Figure 2. Calibrations of (a) MTSAT and (b) FY-2C 0.72-µm channels against *Aqua* MODIS 0.64 channel during TWP-ICE period.

respectively, for the TWP-ICE period. The scatter in the data is a bit larger for MTSAT than for the FY2C. Other types of fits, such as a principal component analysis and force fit to space count, are given on the plots.

The scatter plots and regression fits for the 3.8-µm channels are plotted in Figure 3 separately for day (MTSAT) and night (FY2C). The calibrations apparently changed on both satellites during the course of the experiment, so two calibrations are given for each satellite. Before February 15 (day 46, Figure 3a) the MODIS temperatures were considerably higher than their MTSAT counterparts requiring the application of the following correction:

$$T_M(3.8) = 1.039\ T_{MT}(3.8) - 1.22\ \text{K}, \tag{3}$$

where T is the brightness temperature and the subscripts, M and MT, refer to MODIS and MTSAT, respectively. After day 45 (Figure 3b), the correction is minimal,

$$T_M(3.8) = 0.949\ T_{MT}(3.8) + 15.47\ \text{K}. \tag{4}$$

Before day January 17 (Figure 3c), the FY2C 3.8-µm channel ran slightly warmer than MODIS with

$$T_M(3.8) = 1.241\ T_F(3.8) - 71.77\ \text{K}, \tag{5}$$

where the subscript, F, refers to FY2C. After January 16,

$$T_M(3.8) = 0.9585\ T_F(3.8) + 13.85\ \text{K}. \quad (6)$$

The FY2C channel was extremely noisy for temperatures below 269 K at night (not shown), further limiting its utility. Differences between the 10.8 and 12.0-µm channels were negligible, so no changes are recommended for those channels on either GEOsat. Since TWP-ICE, the navigation of the operational MTSAT data has been improved.

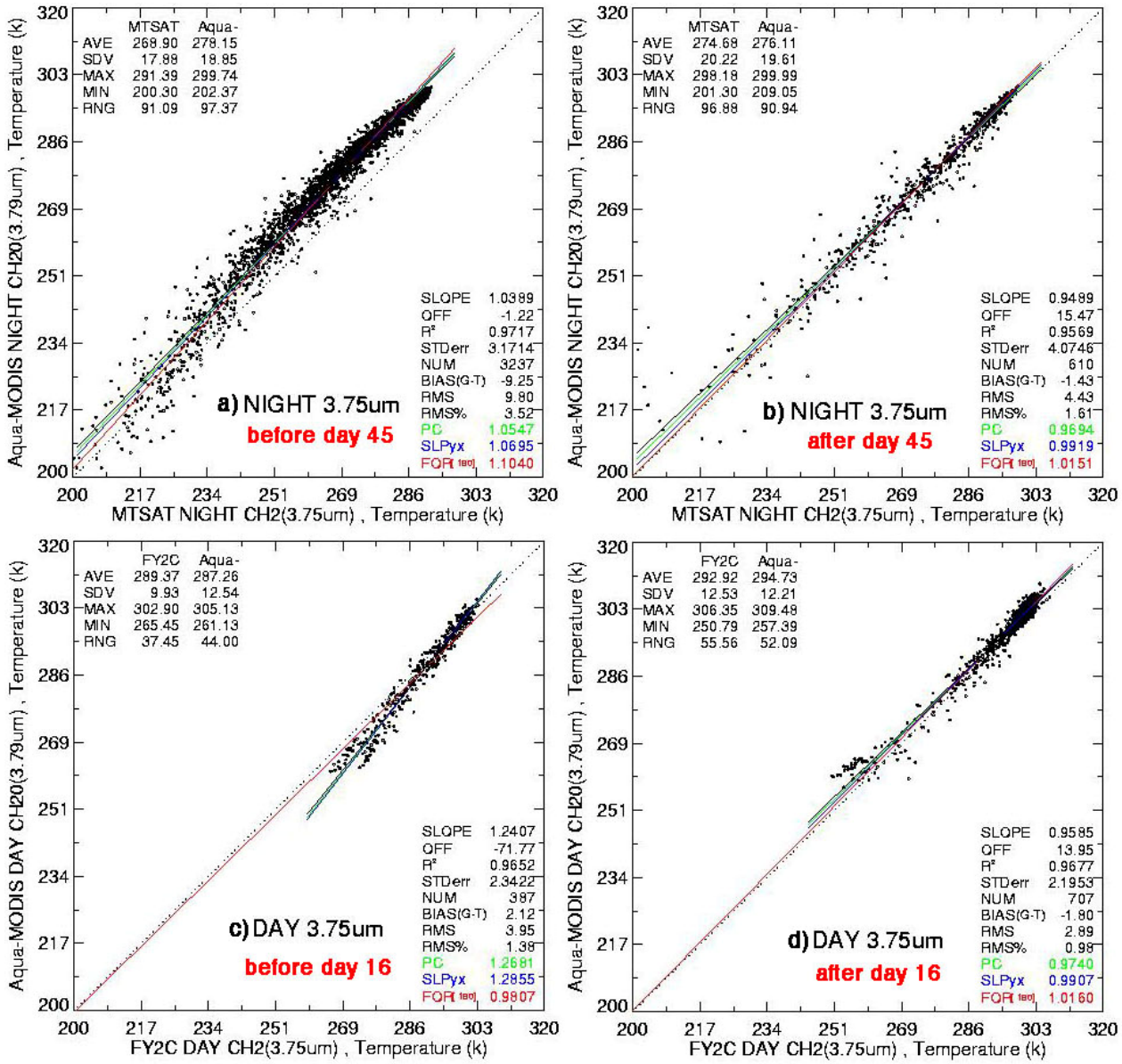

Figure 3. Calibrations of (a, b) nighttime MTSAT and (c, d) daytime FY-2C 3.8-µm channels against *Aqua* MODIS 3.8-µm channel during TWP-ICE period.

The data were processed in near-real time during TWP-ICE using earlier calibrations and reprocessed shortly after the experiment using the calibrations noted above. The results along with imagery and other information were made available at the following website, http://www-angler.larc.nasa.gov/twpice (Phan et al. 2004). The interface for accessing the data is illustrated in Figure 4.

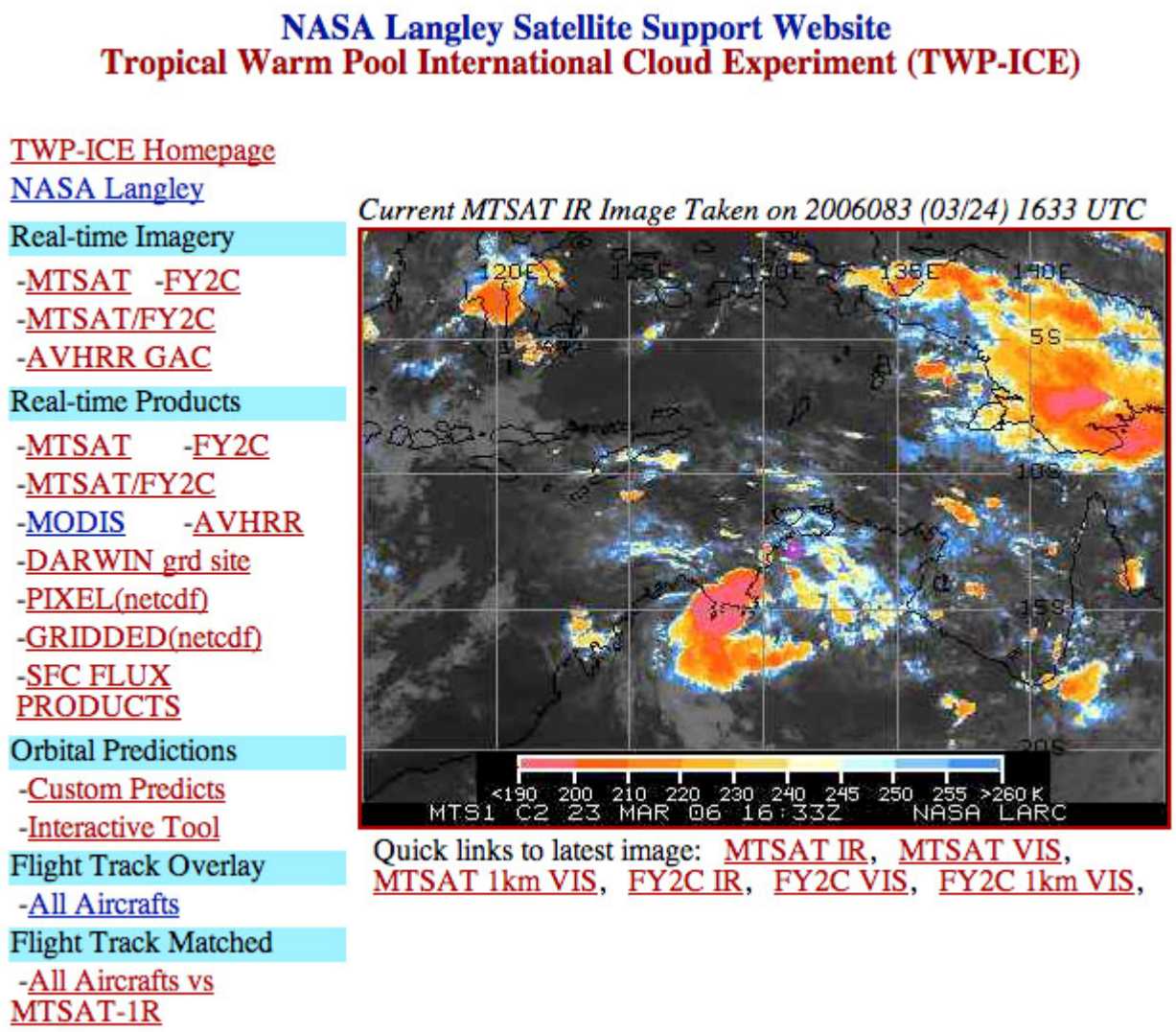

Figure 4. Image of Langley TWP-ICE web page for accessing satellite imagery and cloud products.

The available pixel-level products are summarized in Table 1. The latitude, longitude, solar zenith angle, viewing zenith angle, and relative azimuth angle are denoted by LAT, LON, SZA, VZA, and RAZ, respectively. Averages are also produced on a 1.0° grid. In addition to all of the pixel-level products, surface longwave and shortwave fluxes are also provided. These parameters are also averaged within circles with radii of 10 and 20 km centered on the Darwin surface site and along the flight tracks of the various aircraft. These can be accessed at the website via the links indicated in Figure 4. For

Table 1. VISST output parameters for each pixel.
LAT, LON, SZA, VZA, RAZ
Scene ID (Clear or Phase)
Clear-sky effective temperature
Cloud effective temperature
Cloud effective height and pressure
Cloud top height
Cloud thickness (base height)
Cloud emissivity
Cloud water droplet effective radius or ice effective diameter
Cloud optical depth
Cloud liquid water or ice water path
Broadband SW albedo & LW flux
Reflectance or temperature at 0.64, 3.9, 10.8, 12.0 µm

example, clicking on the link under the heading "Flight Track Overlay" will permit viewing of flights on any day during the experiment. Figure 5 plots the flight tracks for 25 January 2006 on an MTSAT VIS image. Data like these are matched as closely as possible in space and time with the satellite pixels. The figure also shows the aircraft altitude and links to more detailed overlays and the aircraft navigation data.

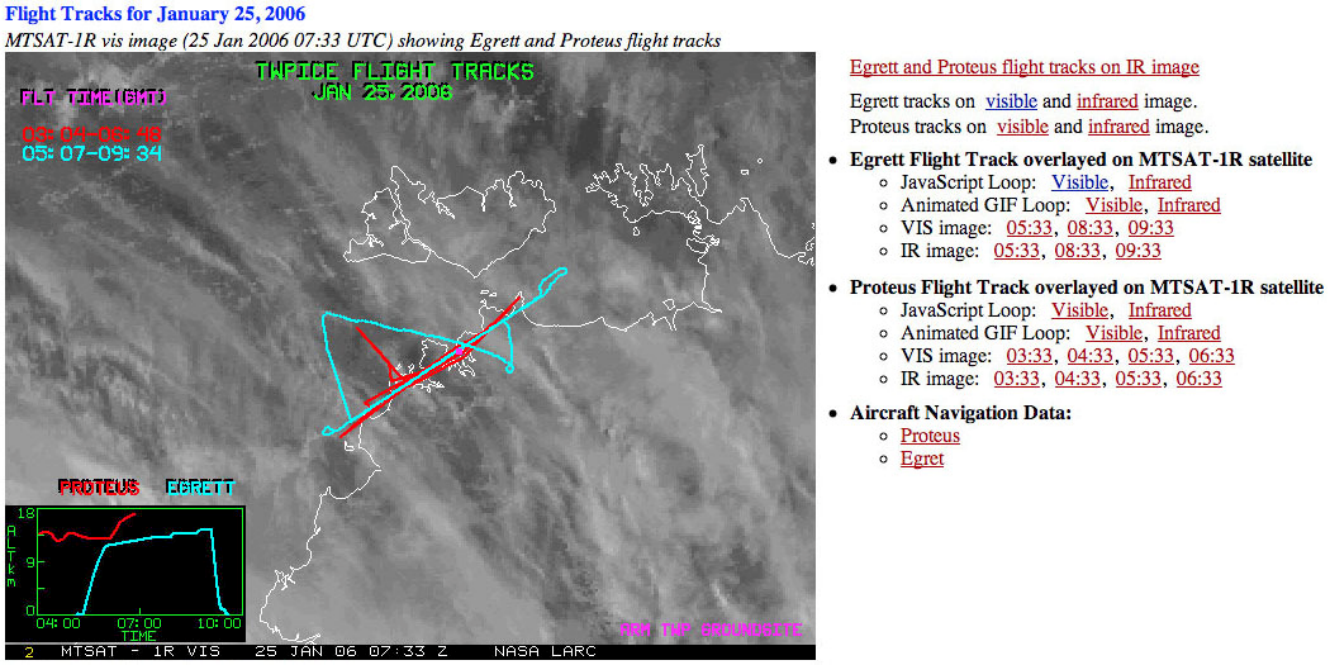

Figure 5. Overlay of Proteus and Egrett flight tracks on MTSAT VIS image taken at 0733 UTC, 25 January 2006. Altitude plot shown in inset. Links to other imagery also indicated on the web page.

Results

Figure 6 shows an example of several pixel-level products derived from data corresponding to the images in Figure 1. The patterns are similar but slightly different owing to the different resolutions, perspectives, times, geographical coverage, and spectral channels. In addition, the MODIS results are plotted on a different color scale, so care should be exercised in comparing the results. The location of Darwin is shown as a magenta square to assist in properly comparing the results at a given location. The NOAA-16 AVHRR (left) and MODIS (right) both view the area at a greater VZA than MTSAT (center) resulting in less space between the high altitude clouds because of foreshortening. The cloud-top heights (top row) are all very similar for the high clouds, but differ considerably for the low and middle clouds. The MODIS analysis uses profiles from the Global Modeling Assimilation Office GEOS 4.03 (DAO 1997) reanalyses instead of the Global Forecast Systems values. The optical depths (center row) from the AVHRR are generally larger than the MTSAT values for optically thick clouds, but are similar for the thinner clouds. The MODIS and MTSAT optical depths are similar at all thicknesses. The intercalibration between MODIS and NOAA-16 has not yet been applied to these results. The patterns in De (bottom row) are also similar, but the NOAA-16 retrievals are generally smaller than the MTSAT values for optically thick clouds. The MODIS values appear to be somewhat larger than their MTSAT counterparts.

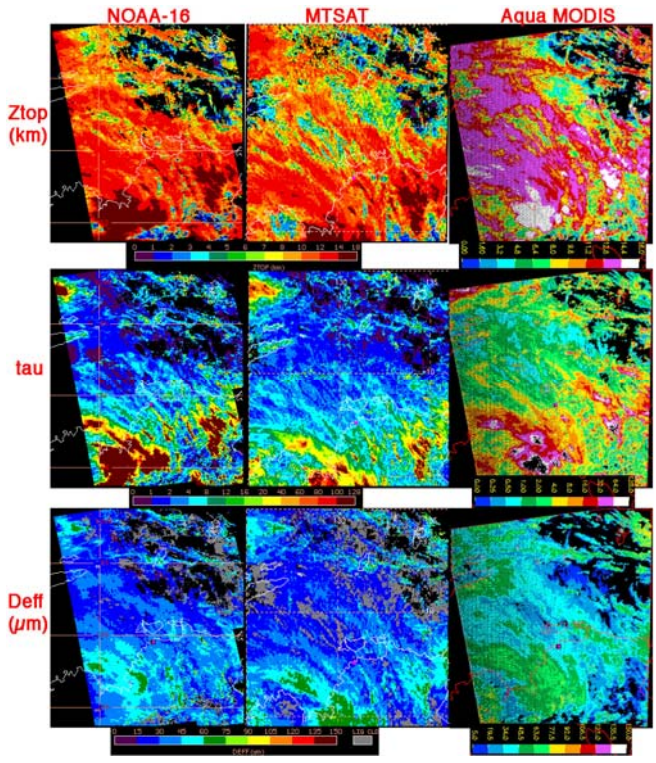

Figure 6. Cloud properties from images in Figure 1. Note scale changes for MODIS and slight differences in geolocation.

The assessment of the results and understanding of the differences between the satellites has just begun. Figure 7 shows a comparison of the MTSAT-derived cloud-top heights and the outline of the clouds passing over Darwin (top) during 19 January derived from the ARM millimeter cloud radar (MMCR). The error bars indicate the variation of top height within the 20-km radius averaging circle. The retrieved cloud OD is shown in the bottom panel for comparison. Night extends from ~0800 to 2000 UTC. The VISST and SIST cloud-top heights are generally within 1 km of the cloud top indicated by the MMCR. Generally, OD tracks with the intensity of the radar reflectivity. Minimum OD occurs around 1800 UTC when the cloud noticeably thins.

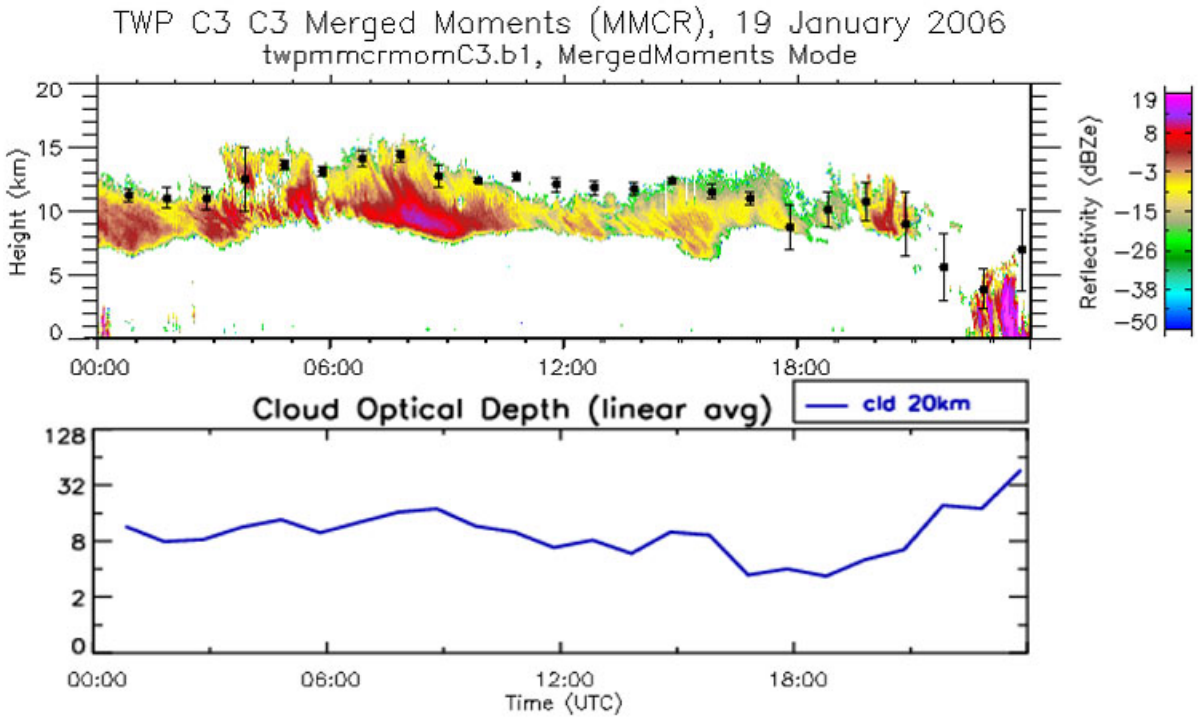

Figure 7. Comparison of MTSAT cloud heights with Darwin MMCR reflectivities (top) with derived MTSAT-derived optical depth (bottom), 19 January 2006.

The clouds that passed over Darwin during 25 January (Figure 6) were thinner, on average, than those during the 19th as seen in Figure 8 (bottom), which shows that the mean MTSAT-derived OD mostly varied between 3 and 4 during the entire day. The cloud-top heights again are within 1 km of the MMCR-derived values in most instances, but the cloud bases are typically too low. However, the MMCR does not provide the entire picture of the cloud boundaries. The ARM micropulse lidar (Figure 9) reveals that the cloud tops extended beyond 16 km in some cases (e.g., 1400 UTC) while the MMCR did not detect tops above 15 km. Although the MMCR and micropulse lidar cloud tops were not very different during 19 January, it is clear that returns from both instruments should be considered when validating the satellite retrievals.

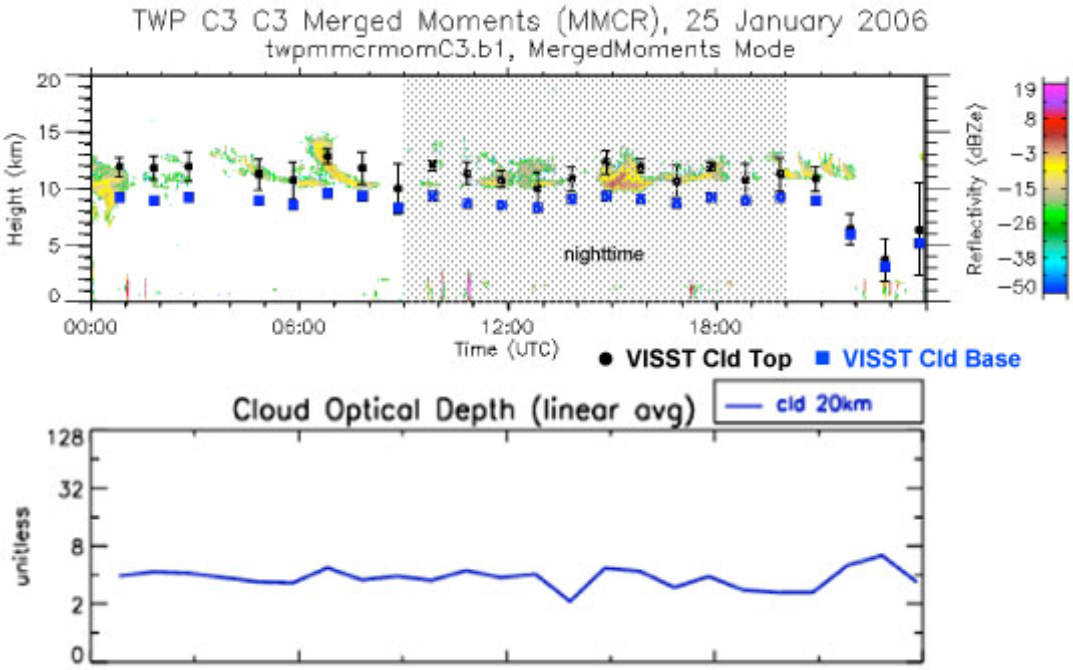

Figure 8. Comparison of MTSAT cloud heights with Darwin MMCR reflectivities (top) with derived MTSAT-derived optical depth (bottom), 25 January 2006 (see figures 1, 5, and 6).

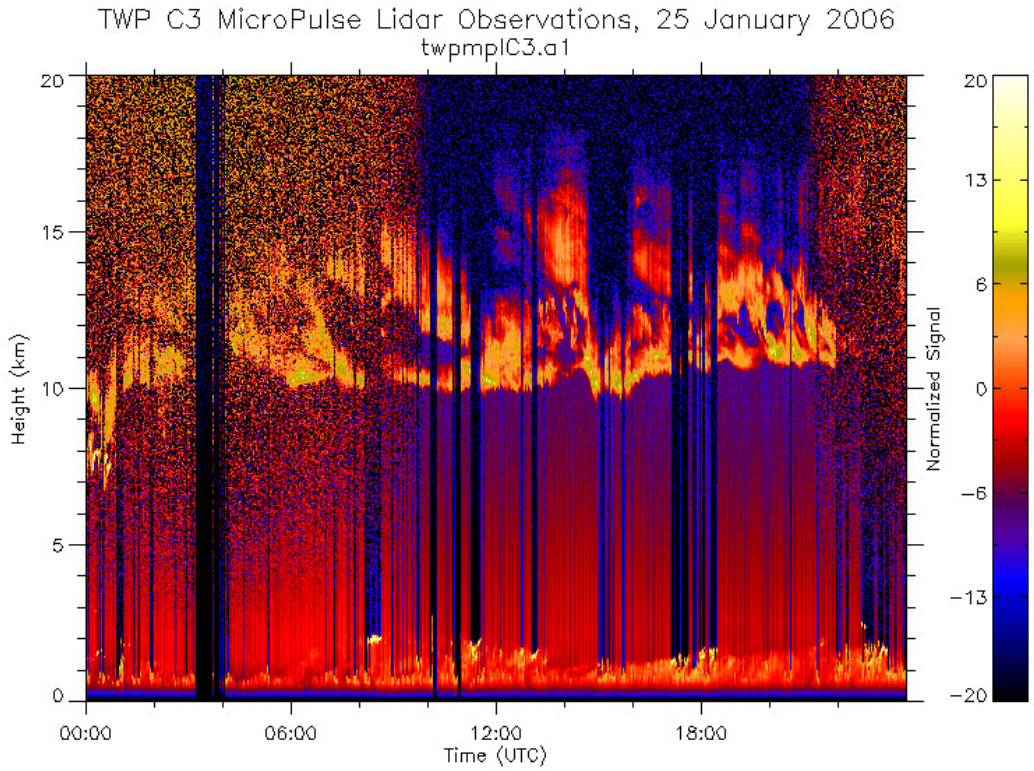

Figure 9. Image of ARM Darwin micropulse lidar normalized returns for 25 January 2006.

Summary and Future Work

Initial analyses have been performed for all available NOAA, *Terra, Aqua,* MTSAT, and FY2C data during TWP-ICE. All image overlays and averages available over Darwin CART and along all flight track paths based on initial calibrations. Early comparisons with ground data appear quite reasonable. Data from the first reprocessing have been archived.

All data will be reanalyzed again using the final calibrations and narrowband-broadband conversions. Additional parameters such as radar overlays will be provided. New retrieval models will be used to account for large differences between the current 0.65-µm model and the MTSAT/FY-2C 0.73-µm channel. Additional comparisons will be made with aircraft and surface data to further validate the results. The satellite analyses should be valuable for understanding the larger scale variations and processes affecting the development and dissipation of convective systems that occurred during TWP-ICE. All ARM Science Team members are encouraged to use the data.

Acknowledgments

This research was sponsored by an Interagency Agreement with Brookhaven National Laboratory supported by the Department of Energy ARM Program.

References

DAO. 1997. GEOS-3 Data Assimilation System Architectural Design. DAO Office Note 97-06. Data Assimilation Office, Goddard Space Flight Center, Greenbelt, Maryland 20771.

Minnis, P., et al. 1995. "Cloud Optical Property Retrieval (Subsystem 4.3)." In *Clouds and the Earth's Radiant Energy System (CERES) Algorithm Theoretical Basis Document*, Vol. III: Cloud Analyses and Radiance Inversions (Subsystem 4), NASA RP 1376 Vol. 3, edited by CERES Science Team, pages 135-176.

Minnis, P, DP Garber, DF Young, RF Arduini, and Y Takano. 1998. "Parameterization of reflectance and effective emittance for satellite remote sensing of cloud properties." *Journal of Atmospheric Science* 55:3313-3339.

Minnis, P, L Nguyen, DR Doelling, DF Young, WF Miller, and DP Kratz. 2002a. "Rapid calibration of operational and research meteorological satellite imagers, Part I: Evaluation of research satellite visible channels as references." *Journal of Atmospheric and Oceanic Technology* 19:1233-1249.

Minnis, P, L Nguyen, DR Doelling, DF Young, WF Miller, and DP Kratz. 2002b. "Rapid calibration of operational and research meteorological satellite imagers, Part II: Comparison of infrared channels." *Journal of Atmospheric and Oceanic Technology* 19:1250-1266.

Minnis, P, WL Smith, Jr., DF Young, L Nguyen, AD Rapp, PW Heck, and MM Khaiyer. 2002c. "Near-real-time retrieval of cloud properties over the ARM CART area from GOES data." In *Proceedings of the Twelfth ARM Science Team Meeting*, April 8-12, St. Petersburg, Florida.

Minnis, P, WL Smith, Jr., L Nguyen, DA Spangenberg, PW Heck, R Palikonda, JK Ayers, C Wolff, and JJ Murray. 2004. "Near-real time cloud properties and aircraft icing indices from GEO and LEO satellites." In *Proceeding of SPIE Forty-ninth Annual Meeting, Weather and Environmental Satellites Conference*. Denver, Colorado, August 2-3 5549, 145-155.

Phan, D, DA Spangenberg, R Palikonda, MM Khaiyer, ML Nordeen, L Nguyen, and P Minnis. 2004. "Web-based satellite products database for meteorological and climate applications." In *Proceedings of the Thirteenth American Meteorological Society Conference Satellite Oceanography and Meteorology*, Norfolk, Virginia, September 20-24, CD-ROM, P8.2.